

## Electrical impedance spectroscopy as a potential tool for recovering bone porosity

C Bonifasi-Lista<sup>1</sup> and E Cherkaev<sup>2</sup>

<sup>1</sup> Bioengineering Department, University of Utah, 72 South Central Campus Drive, Room 2646, Salt Lake City, UT 84112, USA

<sup>2</sup> Department of Mathematics, University of Utah, 155 South 1400 East, JWB 233, Salt Lake City, UT 84112, USA

E-mail: [cb28@utah.edu](mailto:cb28@utah.edu) and [elena@math.utah.edu](mailto:elena@math.utah.edu)

Received 12 November 2008, in final form 27 March 2009

Published 27 April 2009

Online at [stacks.iop.org/PMB/54/3063](http://stacks.iop.org/PMB/54/3063)

### Abstract

This paper deals with the recovery of porosity of bone from measurements of its effective electrical properties. The microstructural information is contained in the spectral measure in the Stieltjes representation of the bone effective complex permittivity or complex conductivity and can be recovered from the measurements over a range of frequencies. The problem of reconstruction of the spectral measure is very ill-posed and requires the use of regularization techniques. We apply the method to the effective electrical properties of cancellous bone numerically calculated using micro-CT images of human vertebrae. The presented method is based on an analytical approach and does not rely on correlation analysis nor on any *a priori* model of the bone micro-architecture. However the method requires *a priori* knowledge of the properties of the bone constituents (trabecular tissue and bone marrow). These properties vary from patient to patient. To address this issue, a sensitivity analysis of the technique was performed. Normally distributed random noise was added to the data to simulate uncertainty in the properties of the constituents and possible experimental errors in measurements of the effective properties. The values of porosity calculated from effective complex conductivity are in good agreement with the true values of bone porosity even assuming high level errors in the estimation of the bone components. These results prove the future potential of electrical impedance spectroscopy for *in vivo* monitoring of level and treatment of osteoporosis.

(Some figures in this article are in colour only in the electronic version)

## 1. Introduction

Osteoporosis is defined as an abnormal loss of bone mineral density (hydroxyapatite crystals) that leads to a deterioration of the bone microstructure and hence a decrease of bone strength. Today, according to the World Health Organization, bone mineral density (BMD) measurements is the standard to address the risk of osteoporotic fracture. However, bone mineral density is only one of the factors affecting bone quality which characterizes the ability of bone to withstand fracture (Hernandez 2006), and some patients diagnosed with osteoporotic fractures have the same or greater bone mineral density than a normal patient (Speller *et al* 1989). This is due to the fact that osteoporosis also involves a loss of structural stability due to an increase of porosity. This important issue has not yet been addressed successfully. The current standards in the assessment of osteoporosis are based on photon absorptiometry techniques (dual x-ray absorptiometry or DXA). Quantitative ultrasound (QUS) measurements are emerging as an alternative to radiation techniques and they are being used for monitoring anti-osteoporotic treatments in prospective trials (Prins *et al* 1998). QUS techniques are safer and cheaper than radiation techniques. One of the drawbacks of ultrasound techniques in bone is the fact that sound waves lose energy too fast as they travel through bone and they do not penetrate it very deep. Recently, electrical measurements done in bovine trabecular bone samples showed excellent correlations between electric and mechanical properties and BMD measurements (Sierpowska *et al* 2003). The authors found that the electric parameters predicted mechanical characteristics of bovine bone better than the broadband ultrasound attenuation (BUA) measurements. Dielectric permittivity showed strong linear correlations with bone mineral density measurements ( $r = 0.866$ ,  $p < 0.01$  at 50 kHz). Measurements of electrical properties of trabecular bone were highly reproducible over a wide range of frequencies, being strongly dependent on the frequency and site. Using numerical simulations, sensitivity of impedance measurements to bone density variations was shown in Katz *et al* (2006). Lately, good correlations between dielectric and mechanical properties of human trabecular bone were reported (Sierpowska *et al* 2005). The relative permittivity showed the strongest linear correlations with Young's modulus ( $r = 0.71$ ,  $p < 0.01$ ) and ultimate strength ( $r = 0.73$ ,  $p < 0.01$ ) at a frequency of 1.2 MHz. Conductivity was found to be a poor estimate of BMD. Conductivity is due to ion movements through the fluid phase and may change without any change in mineral density (Williams and Saha 1996). However, both conductivity and permittivity as well as mechanical properties do depend on the geometry of the microstructure (Sierpowska *et al* 2007). These studies indicate the potential of impedance spectroscopy for the evaluation of bone quality.

The inverse homogenization method developed recently for electromagnetic measurements allows us to estimate the parameters of the microstructure of a two-component composite medium using measurements of the effective complex permittivity of the composite material (Cherkaev 2001). The method is based on reconstruction of the spectral measure in the Stieltjes analytic representation of the effective permittivity developed in Bergman (1978), Milton (1980) and Golden and Papanicolaou (1983) for composites with a periodic or random microstructure. The spectral measure contains all information about the microgeometry. It was shown in Cherkaev (2001) that the spectral measure can be uniquely recovered from the measurements of the effective property over a range of frequencies, but the problem of reconstruction is very ill-posed and requires regularization. After reconstruction of the spectral function, geometric parameters can be calculated. In particular, the volume fraction of one of the components in the composite equals the zero moment of the spectral function. Higher order moments contain further microstructural information (Bergman 1978, Bergman 1993, Golden and Papanicolaou 1983). This method is valid for a wide range of physical properties such

**Table 1.** Recovering bone porosity using several inverse analytic methods that assume an idealized microgeometry and comparison with the spectral measure method (SMM) proposed here.

Method	$P_{\text{true}} = 92.60$		$P_{\text{true}} = 89.87$	
IMG	99.31	98.39	98.66	97.25
	99.54	98.90	99.10	98.11
⊥	74.95	78.24	60.77	67.56
SMM	92.77	92.75	89.67	89.51

as electrical and thermal conductivity, diffusivity, elastic and viscoelastic material properties, and can be used for composites of periodic or random microgeometry. The method was successfully applied to the estimation of brine volume in sea ice from measurements of its complex permittivity in Cherkaev and Golden (1998), where comparison with the laboratory measurements of the brine volume of sea ice demonstrated an excellent agreement. The spectral function was reconstructed from effective measurements in Gajdardziska-Josifovska *et al* (1989a), Day and Thorpe (1999), Day *et al* (2000), Cherkaev (2003), Cherkaev and Zhang (2003), Tuncer (2005) and Zhang and Cherkaev (2008).

A straightforward way to obtain the volume fractions of the components from given measured effective permittivity and the permittivities of the bone constituents, seems to invert some of the known mixture formulae. Indeed, an analytic mixture formula which gives the effective permittivity as a function of permittivity and fractions of the materials in the composite can be ‘inverted’ to give the volume fractions. However, this approach does not result in accurate estimates of the volume of the components in the composite. An example of this inaccuracy was demonstrated in Zhang and Cherkaev (2008) with the ‘inverse Maxwell–Garnett formula’ applied to effective permittivity values analytically calculated for several elliptic cylinder microgeometries. The estimated volume fractions ranged from 12.8–26.1 for true porosity 18%, to 26.5–46.4 for the porosity 35%. In table 1 we summarize the results of numerical simulations using several inverted for volume fraction analytic formulae, to demonstrate that this straightforward approach does not work efficiently for the evaluation of bone porosity. We considered three different idealized microgeometries whose analytic representation is known: (1) microgeometry idealized as a matrix with spherical inclusions whose effective permittivity is given by the Maxwell–Garnett formula (MG), (2) laminates with an interface parallel to the applied field (||), and (3) a microgeometry consisting of laminates with an interface perpendicular to the applied field (⊥). We inverted these analytic formulae to obtain analytic formulae for calculating porosity and applied them to the bone effective permittivity. We used the effective permittivity values for real bone microgeometry computed using COMSOL; the forward computation is described in section 4.1. The calculated porosity estimates are summarized in table 1. The first three rows show estimates obtained using the inverse analytic formulae: an inverse Maxwell–Garnett formula (IMG) and inverse formulae for parallel (||) and perpendicular (⊥) laminates. The last row shows porosity calculated using the spectral measure method (SMM) proposed here, which does not assume any particular geometry. The results are shown for two samples with true porosity  $P_{\text{true}} = 92.60$  and  $P_{\text{true}} = 89.87$ . The two columns under each heading give the porosity calculated using data at the frequency  $\omega = 10$  Hz and  $\omega = 10^5$  Hz. For the SMM method, these columns give a range of estimated values. The results clearly show that inverse analytic formulae are not able to provide a good estimate for porosity. This motivates the development of a different approach to the estimation of volume fractions of constituents in the composite based on inverse homogenization.

The technique of inverse homogenization was extended to viscoelastic properties in Bonifasi-Lista and Cherkaev (2006). Recently, this technique was successfully used to recover bone porosity from measurements of the effective complex shear modulus of bone in Bonifasi-Lista and Cherkaev (2008). In this paper, we present the potential of the inverse homogenization technique to recover the porosity of bone, an important factor besides BMD measurements in addressing bone quality, from effective complex conductivity measurements.

## 2. Spectral representation of the effective permittivity of a heterogeneous medium

A Stieltjes function with special analytical properties representing the effective complex permittivity of a two component composite was introduced by Bergman (1978). The Stieltjes integral representation can be derived from a spectral representation of an operator using spectral theory of self-adjoint linear operators, and under certain mathematical conditions it is unique (Lax 2002). Its general form is as follows:

$$F(s) = \int \frac{d\eta}{s - t}, \quad (1)$$

where  $s$  is a complex variable, the spectral function  $\eta$  is a non-negative measure of the finite total mass on real line. Bergman (1978) determined a spectral representation for the effective complex permittivity of two-component composite material exploiting the properties of the effective parameter as an analytic function of the ratio of the component parameters. The complex variable  $s$  was defined in terms of the complex permittivity of the constituents in the mixture and the function  $F(s)$  in terms of the effective complex permittivity of the heterogeneous medium and the permittivity of one of the constituents. For a two-component composite, this representation has the following form (Bergman 1978, Milton 1979, Golden and Papanicolaou 1983, Bergman 1993):

$$F(s) = 1 - \frac{\epsilon_{\text{eff}}}{\epsilon_2} = \int_0^1 \frac{d\eta(t)}{s - t} \quad \text{with} \quad s = \frac{1}{1 - \epsilon_1/\epsilon_2}. \quad (2)$$

Here  $\epsilon_{\text{eff}}$  is the effective complex permittivity of the mixture, and  $\epsilon_i$ ,  $i = 1, 2$ , is the complex permittivity of the  $i$ th constituent. This analytical representation was used to derive bounds for the effective complex permittivity of a composite formed of two given materials (Bergman 1978, Milton 1979, Bergman 1980, Milton 1981, Golden and Papanicolaou 1983, Bergman 1985). The representation is valid for other physical properties such as electrical conductivity, thermal conductivity, diffusivity and elastic properties. The spectral representation (2) separates information about the properties of the constituents (contained in variable  $s$ ) from geometric information about the microstructure which is enclosed in the spectral function  $\eta$ . This specific feature of the representation (2) allows us to use it to derive information about the microgeometry (McPhedran *et al* 1982, McPhedran and Milton 1990, Cherkaeva and Tripp 1996, Cherkaev 2001). The structural information is contained in the moments of the function  $\eta$ . The  $n$ th moment  $\eta_n$  of function  $\eta$  is

$$\eta_n = \int_0^1 t^n d\eta(t). \quad (3)$$

Bergman further proved that the zero moment of the measure  $\eta$  gives the volume fraction of one of the components. Higher order moments give information about the values of the  $n$ -point correlation functions (Bergman 1993); the methods of computing further moments are discussed in Cherkaev and Ou (2008). The analytical representation (2) does not imply any *a priori* model of the microstructure or of the relative arrangement of the constituents and can be used for any two-component composite.

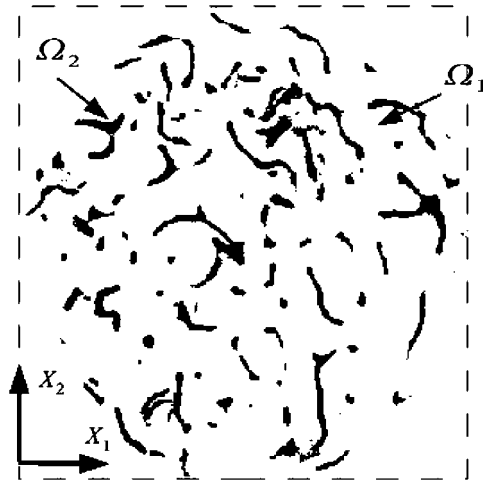


**Figure 1.** Example of a micro-CT scan of a T12 vertebra used in our numerical simulations. Cavities of trabecular tissue ( $\Omega_2$ ) are filled with bone marrow ( $\Omega_1$ ). Micro-CT images are courtesy of Professor Yener N Yeni and his group.

We consider cancellous bone as a heterogeneous medium composed of trabecular tissue with cavities filled with bone marrow (figure 1). We use Maxwell's equations for spatially varying time harmonic fields of frequency  $\omega$  as the equations governing propagation of electromagnetic fields in the medium

$$\nabla \times \mathbf{H}(\mathbf{x}) = \mathbf{J}(\mathbf{x}) + i\omega\mathbf{D}(\mathbf{x}), \quad \nabla \times \mathbf{E}(\mathbf{x}) = -i\omega\mathbf{B}(\mathbf{x}). \quad (4)$$

Here  $\mathbf{x}$  is the spatial variable,  $\mathbf{E}$  and  $\mathbf{H}$  are the electric and magnetic fields,  $\mathbf{J}$  is the electric current field and  $\mathbf{D}$  and  $\mathbf{B}$  are, respectively, the displacement and induction fields. These fields are related by the constitutive equations:  $\mathbf{D}(\mathbf{x}) = \epsilon(\mathbf{x})\mathbf{E}(\mathbf{x})$ ,  $\mathbf{B}(\mathbf{x}) = \mu(\mathbf{x})\mathbf{H}(\mathbf{x})$ ,  $\mathbf{J}(\mathbf{x}) = \sigma(\mathbf{x})\mathbf{E}(\mathbf{x})$ , where  $\epsilon = \epsilon_o\epsilon_r$  is the complex permittivity of the medium,  $\epsilon_o$  is the permittivity of free space,  $\epsilon_r$  is the relative permittivity,  $\mu$  is the magnetic permeability and  $\sigma$  represents the conductivity of the medium. Bone tissues as most biologic conductors have the magnetic permeability  $\mu$  close to the permeability  $\mu_o$  of air (Habal and Reddi 1992). Using constitutive equations and applying the divergence operator ( $\nabla \cdot$ ) on both sides of the first equation in (4), we obtain for time harmonic fields

$$\nabla \cdot (\sigma + i\omega\epsilon)\mathbf{E} = 0, \quad \nabla \times \mathbf{E} + i\omega\mu_o\mathbf{H} = 0. \quad (5)$$

Combining conductivity and permittivity in complex permittivity  $\epsilon^*$  and complex conductivity  $\sigma^*$

$$\epsilon^* = \epsilon - i\sigma/\omega \quad \text{and} \quad \sigma^* = \sigma + i\omega\epsilon = i\omega\epsilon^* \quad (6)$$

we rewrite the first of equations (5) in terms of  $\epsilon^*$  or  $\sigma^*$ , as follows:

$$\nabla \cdot \epsilon^*(\mathbf{x})\mathbf{E}(\mathbf{x}) = 0 \quad \text{or} \quad \nabla \cdot \sigma^*(\mathbf{x})\mathbf{E}(\mathbf{x}) = 0 \quad (7)$$

Note that for low frequency, the response of material is mostly influenced by the values of the conductivity parameter and the contribution of the capacitive component (or the dielectric parameter) is small, whereas for high frequency, the response is determined by the permittivity and the influence of the conductivity is negligible. Generally, the permittivity  $\epsilon$  itself is a complex function of frequency  $\omega$ .

Cancellous bone is a heterogeneous medium; it has a porous structure formed by trabeculae and filled by bone marrow. Trabecular tissue and bone marrow are characterized by different values of electric and dielectric parameters; therefore, complex conductivity  $\sigma$  depends not only on frequency but also on spatial coordinate  $\mathbf{x}$ . Let function  $\chi = \chi(\mathbf{x})$  be the characteristic function of domain  $\Omega_1$  occupied by bone marrow tissue which takes values 1 if  $\mathbf{x} \in \Omega_1$  and zero if  $\mathbf{x} \in \Omega_2$ , where  $\Omega_2$  is the region occupied by the trabecular tissue. Then the spatial dependence of complex conductivity in the domain  $\Omega = \Omega_1 \cup \Omega_2$  can be expressed as  $\sigma^*(\mathbf{x}) = \chi(\mathbf{x})\sigma_1^* + (1 - \chi(\mathbf{x}))\sigma_2^*$  with  $\sigma_i^*, i = 1, 2$ , being the complex conductivity of bone marrow and trabecular tissue, respectively.

The wavelength of the electric current used in clinical applications is much larger than the scale of the structure of the trabecular bone. Various mechanical models of cancellous bone have been developed based on homogenization of materials with the microstructure. They are used in the computations of effective mechanical properties of bone, its static and dynamic responses (Tokarzewski *et al* 2001). Since the applied current has a very large wavelength in comparison with the fine scale bone structure, only an averaged or homogenized response to the applied electromagnetic excitation can be measured. This situation can be modeled by assuming that the second term of the second equation in (5) is negligible and the electric field is curl free. This allows us to represent the electric field as  $\mathbf{E} = \nabla\phi$  for some potential  $\phi$ , which satisfies the equation

$$\nabla \cdot \sigma^*(\mathbf{x})\nabla\phi(\mathbf{x}) = 0 \quad \text{in} \quad \Omega. \quad (8)$$

In our numerical simulations, we use equation (8) as the governing equation.

Complex conductivity  $\sigma^*(\mathbf{x})$  is a spatially oscillating function, and we use the two-scale asymptotic expansions technique of homogenization theory to derive equations for the effective complex permittivity. The derivation is presented in appendix A. The effective parameter is a coefficient of proportionality between the averaged electric current  $\mathbf{J}$  and averaged electric field  $\mathbf{E}$  (Hashin 1972)

$$\langle \mathbf{J} \rangle = \sigma_{\text{eff}}^* \langle \mathbf{E} \rangle. \quad (9)$$

Here,  $\mathbf{J}(\mathbf{x}) = \sigma^*(\mathbf{x})\mathbf{E}(\mathbf{x})$ , and  $\sigma_{\text{eff}}^*$  is the effective complex conductivity of the trabecular bone structure. The averaging operator  $\langle \cdot \rangle$  is the mean operator which for any function  $f$  is given by

$$\langle f \rangle = \int_{\Omega} f(\mathbf{x}) \, dV. \quad (10)$$

In appendix A, we sketch the derivation of the Stieltjes representation of the effective complex conductivity of a heterogeneous medium using homogenization theory (two-scale asymptotic expansion) and spectral decomposition.

In the case considered here, complex variable  $s$  depends on the components of the medium,  $\sigma_1^*$  and  $\sigma_2^*$ , that are, respectively, the complex conductivity of bone marrow and trabecular tissue. Expressing  $s$  in terms of  $\sigma_1^*$  and  $\sigma_2^*$  we have

$$s = \frac{\sigma_2^*}{(\sigma_2^* - \sigma_1^*)} = \frac{i\omega\epsilon_2^*}{(i\omega\epsilon_2^* - i\omega\epsilon_1^*)} = \frac{\epsilon_2^*}{(\epsilon_2^* - \epsilon_1^*)}. \quad (11)$$

We end up with spectral representation similar to (2)

$$F(s) = 1 - \frac{\sigma_{\text{eff}}^*}{\sigma_2^*} = 1 - \frac{\epsilon_{\text{eff}}^*}{\epsilon_2^*} = \int_0^1 \frac{d\eta(t)}{s - t}. \quad (12)$$

Since complex conductivity  $\sigma_i^*, i = 1, 2$ , of the constituents of the medium and the effective complex conductivity depend on frequency  $\omega$ , the complex variable  $s$  and the analytical

function  $F(s)$  depend on frequency as well. Function  $F(s)$  can be easily constructed from experimental data measured for different frequencies. Then, the function  $\eta$  can be recovered from integral equation (12). Once the spectral function  $\eta$  is reconstructed, the porosity  $P$  is obtained as zero moment of  $\eta$  by (3)

$$P = \int_0^1 d\eta(t). \quad (13)$$

The porosity  $P$  of bone is understood as the volume fraction of bone marrow.

### 3. Reconstruction of the spectral measure $\eta$

This section discusses a problem of reconstruction of microstructural information and the spectral function  $\eta$ . The problem of extraction of microstructural information was first introduced in McPhedran *et al* (1982); McPhedran and Milton (1990) for the estimation of volume fraction of one component in a two-component mixture from the measurements of the effective complex permittivity of the composite material. An analytical approach to the calculation of volume fraction of one of the materials in the composite was developed in Cherkaeva and Tripp (1996) and Tripp *et al* (1998) and extended to the problem of recovering bounds on the microstructural parameters for isotropic composite materials in Cherkaev and Golden (1998). This analytical method allows us to estimate the volume fraction of one component of the mixture exploiting the analytical representation given by (2). Explicit formulae for the bounds on the volume fraction of one of the constituents are derived in Cherkaev and Golden (1998). Application of the method to the evaluation of brine volume from experimentally measured complex permittivity of sea ice in Golden *et al* (1998) demonstrated a good agreement of the calculated brine volume with experimentally measured volume of brine. For a set of data with brine volume  $p_1 = 0.036$ , the calculated bounds are  $0.0333 \leq p_1 \leq 0.0422$ . For the data set with brine volume  $p_2 = 0.0205$ , the bounds for the brine volume are  $0.0189 \leq p_2 \leq 0.0213$ . It was shown in Cherkaev (2001) that the spectral function  $\eta$  in the integral representation (2) can be uniquely reconstructed if measurements of the effective properties of the composite are given along some arc on the complex plane  $s$ . Such data can be obtained from measurements in an interval of frequency provided that at least one of the constituents is frequency dependent (Cherkaev 2001). This method, called inverse homogenization, was extended to the viscoelastic problem in Bonifasi-Lista and Cherkaev (2006) and used successfully to recover the porosity of bone from the measurements of effective shear modulus (Bonifasi-Lista and Cherkaev 2008).

Function  $\eta$  can be reconstructed directly from complex-valued function  $F(s)$  using integral equation (12) or either from a real or imaginary part of it. Separating real and imaginary parts of function  $F(s)$  and using  $s = x + iy$ , we obtain

$$\operatorname{Re}(F(s)) = \int_0^1 \frac{(x-t) d\eta(t)}{(x-t)^2 + y^2}, \quad \operatorname{Im}(F(s)) = - \int_0^1 \frac{y d\eta(t)}{(x-t)^2 + y^2}. \quad (14)$$

The reconstruction problem is equivalent to the inverse potential problem, which is an ill-posed problem. Practically this means that small variations in the data or computational noise in a numerical algorithm can lead to arbitrary large variations of the solution. To construct a regularized solution, the problem is discretized and the minimization problem is formulated. To deal with the ill-posedness of the problem, we introduce a stabilization functional which constrains the set of minimizers. We reformulate the problem as an unconstrained minimization using a Lagrange multiplier. In the case of a quadratic stabilization functional, the minimization problem takes the following form equivalent to the Tikhonov

regularization with the regularization parameter  $\alpha$ :

$$\min_{g \in R^n} \{ \|Kg - f\|_2^2 + \alpha \|g\|_2^2 \} \quad (15)$$

Here  $K$  is the discretization of a real or imaginary part of  $F(s)$  in integral representation (14). Function  $f$  is either a real or imaginary part of  $F(s)$  obtained experimentally and  $g$  is the discretization of  $d\eta(t)$ . To find the minimizer of the problem, we solve its Euler equation; the solution is given by

$$g_\alpha = (K^T K + \alpha I)^{-1} K^T f. \quad (16)$$

We use the singular value decomposition (SVD) of nonsymmetric matrix  $K$  given by

$$K_{m \times n} = U_{m \times m} \Sigma_{m \times n} V_{n \times n}^T. \quad (17)$$

Here the matrix  $\Sigma$  is a diagonal matrix with diagonal entries  $s_i$  which are the singular values of  $K$ , and matrices  $U$  and  $V$  are unitary matrices whose column vectors  $u_i$  and  $v_i$  are the left and right singular vectors of  $K$ . Using the pseudoinverse  $K^+$  of  $K$ ,  $K^+ = V \Sigma^+ U^T$  where  $\Sigma^+$  is the transpose of  $\Sigma$  in which  $s_i$  are replaced by  $s_i^{-1}$ , the solution  $g_\alpha$  can be expressed in the form

$$g_\alpha = \sum_{i=1}^m \frac{s_i (u_i^T f)}{s_i^2 + \alpha} v_i. \quad (18)$$

Parameter  $\alpha$  is the regularization parameter that determines the weight of each singular value of  $K$  in the reconstruction of  $g_\alpha$ . Regularized inverse algorithms depend on the regularization parameter  $\alpha$ . The L-curve method (Vogel 2002) was used to choose a proper value for parameter  $\alpha$ . This method consists in plotting the log of the squared norm of the regularized solution,  $\log(\|g_\alpha\|_2)$ , against the log of the squared norm of the regularized residual,  $\log(\|Kg_\alpha - f\|_2)$ , for a range of values of the regularization parameter. This curve typically has an L shape and the proper value of the parameter  $\alpha$  corresponds to the corner of this curve. To find the value of parameter  $\alpha$  we use the method of Hansen and O'Leary (1993) who recommended to pick the point corresponding to the maximal curvature of the curve. Once the function  $\eta$  is reconstructed, the porosity can be easily recovered by (13).

## 4. Results of numerical simulations

### 4.1. Forward problem: simulation of bone effective properties

A series of numerical simulations was performed in order to validate the proposed method. First, we calculated the effective complex conductivity of a sample of trabecular bone. Then using these calculated values as data and employing the developed algorithm, we solved the inverse problem of reconstruction of the spectral function and estimated bone porosity. Comsol Multiphysics, a finite-element-based program, was used to compute the effective complex conductivity of a real sample of trabecular bone with geometry obtained from a micro-CT scan. Micro-CT scans of a T12 vertebra of a 79 year old white male donor were used to model the micro-architecture of the bone. A micro-CT scan of one of the samples is shown in figure 1.

In computational experiments we use (8) as the governing equation. As was described in section 2, the complex conductivity of bone changes on fine scale and can be represented as  $\sigma^*(\mathbf{x}) = \chi(\mathbf{x})\sigma_1^* + (1 - \chi(\mathbf{x}))\sigma_2^*$ , where  $\sigma_i^*$ ,  $i = 1, 2$ , is the complex conductivity of bone marrow and trabecular tissue, respectively. Then the governing equation for the forward problem is

$$\nabla \cdot ((\chi(\mathbf{x})\sigma_1^* + (1 - \chi(\mathbf{x}))\sigma_2^*) \nabla \phi(\mathbf{x})) = 0. \quad (19)$$

The governing equation was implemented using the Comsol FEM code in the frequency domain and solved for a range of frequencies. The computational domain  $\Omega = \Omega_1 \cup \Omega_2$  is a rectangular box shown as a dashed-line rectangle in figure 1. As boundary conditions, a drop of potential  $\phi$  along the  $x_1$ -axis was applied while the net flux on boundaries along the  $x_2$ -axis was kept to zero. Once the spatial distribution of  $\mathbf{E}$  and  $\mathbf{J}$  is calculated numerically, the effective complex conductivity  $\sigma_{\text{eff}}^*$  can be obtained from (9). The effective properties calculated in this way are equivalent to experimentally determined macroscopic properties with boundary conditions of the form  $\phi(\mathbf{x}) = \mathbf{A} \cdot \mathbf{x}$ ,  $\mathbf{x} \in \partial(\Omega)$  for some constant vector  $\mathbf{A}$ .

The values for complex conductivity of trabecular tissue and bone marrow for these numerical simulations were obtained from published experimental data in Gabriel *et al* (1996a, 1996b, 1996c). Complex permittivity properties  $\epsilon_i$  of trabecular bone and bone marrow were obtained using parametric models described in Gabriel *et al* (1996c). These parameterized models are based on Cole–Cole functions given in the frequency domain.

To validate the implementation of the solution of the forward problem for the simulation of the effective properties in the frequency domain using FEM, we considered a model problem. In this model simulation, we assume that the structure is composed of a periodic hexagonal array of circular cylinders embedded in a matrix phase. The unit cell of the cross-section of this hexagonal microgeometry is shown in figure B1. The structure is formed by periodically repeating this cell over a large domain and then shrinking this domain to the size of the domain  $\Omega$ . The hexagonal lattice of circular cylinders represents trabecular tissue embedded in a bone marrow matrix. The effective complex conductivity of this structure is determined by a method proposed by Perrins *et al* (1979) who extended an approach of Lord Rayleigh (1892) to semi-analytically calculate the effective conductivity of circular cylinders arranged in squared or hexagonal periodic arrays. The method exploits symmetries of the geometry and is based on matching analytic solutions of problems with constant parameters. A summary of the derivation of the effective complex conductivity for this hexagonal microgeometry is presented in appendix B.

For the model simulation, we assume that the cylinders are filled with trabecular material and bone marrow fills the region outside the cylinders. The volume fraction of the cylinders is 0.3114 which corresponds to 0.6886 porosity. The effective complex conductivity of this idealized microstructure was numerically calculated using the FEM Comsol code and compared with the analytical solution. Figure 2 shows real and imaginary parts of the effective complex conductivity calculated using these two different methods. The excellent match between the numerical results and the analytical solution justifies further use of the numerical method to calculate the effective properties of the bone structure.

To numerically simulate the data for algorithm validation, effective complex conductivity was determined for four specimens characterized by different microgeometries derived from real 2D micro-CT images. The effective conductivity was computed for 11 different frequencies evenly spaced between  $10^1$  and  $10^{11}$  Hz. Figure 3 shows the effective complex conductivity for one of the specimens.

#### 4.2. Recovery of porosity by solving the inverse problem

The porosity of bone can be recovered from the first moment of the spectral function  $\eta$  as indicated in equation (3). The spectral function  $\eta$  can be reconstructed from either the real or the imaginary part of function  $F(s)$  by the minimization of functional (15). This is equivalent to regularization using a Tikhonov filter as given by (18). In this approach, no *a priori* assumptions about the geometry of the microstructure is needed. Measurements of the effective complex conductivity of cancellous bone in a range of frequencies are used as data.

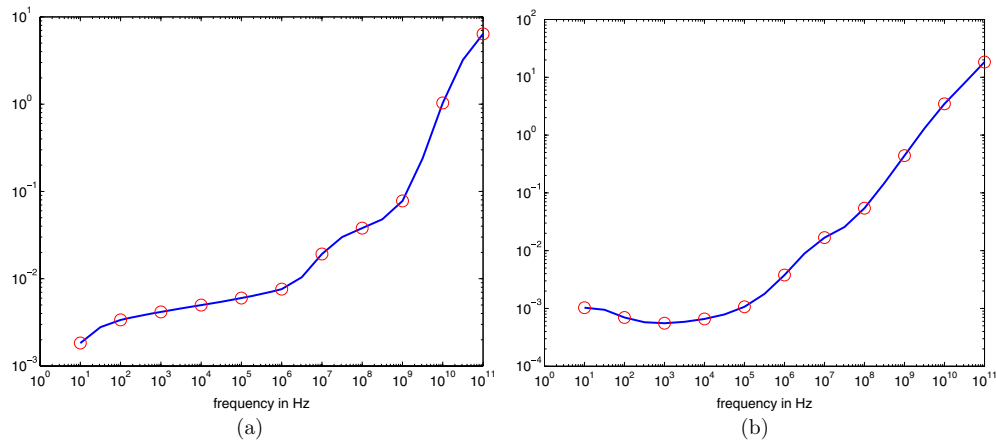


**Figure 2.** Effective complex conductivity of the model structure formed by a hexagonal array of trabecular cylinders embedded in a bone marrow matrix. The analytical solution is shown by a continuous line and the FEM numerical solution is marked by circles  $\circ$ . (a) Real part of complex conductivity. (b) Imaginary part of complex conductivity.

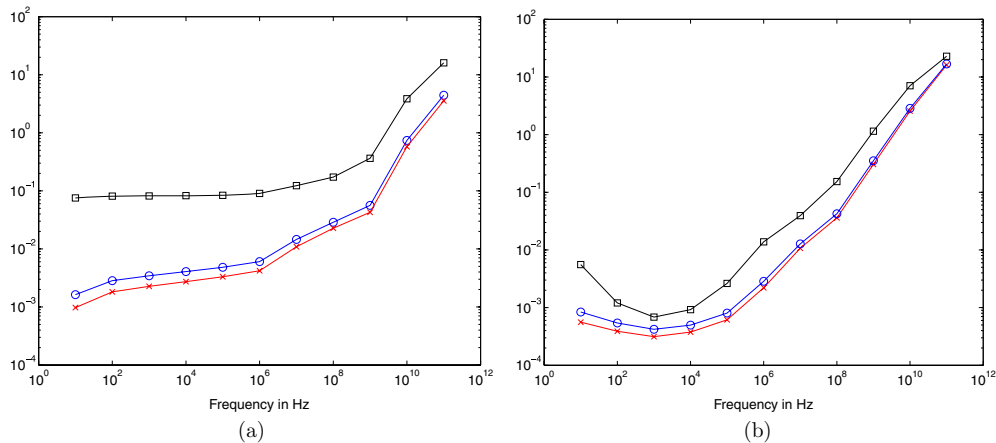


**Figure 3.** Complex conductivity of trabecular bone shown in figure 1. Effective complex conductivity of bone is marked by circles  $\circ$ ; conductivity of trabecular tissues is denoted by squares  $\square$ ; conductivity of bone marrow is indicated by crosses  $\times$ . (a) Real part of the complex conductivity. (b) Imaginary part of the complex conductivity.

This can be determined experimentally *in vivo* or *in vitro*. However, frequency-dependent properties of the constituents of cancellous bone (trabecular and bone marrow) are required as well. There is an undergoing effort to determine and tabulate electrical properties of biological tissues (Gabriel *et al* 1996a, 1996b, 1996c). Unfortunately, biological properties are subject dependent and they can only be approximated with some uncertainty. Moreover, effective properties can be measured with some experimental error. To simulate this situation and to address these issues, different normally distributed random functions were added as ‘noise’ to the complex conductivity properties  $\sigma_i^*$  of the constituents and to the effective conductivity  $\sigma_{\text{eff}}^*$ . Different distributions with zero mean, unit variance and unit standard deviation were used to

**Table 2.** Porosity  $P$  recovered from the real and imaginary parts of function  $F(s)$ .

$P_{\text{true}}$	$P_{\text{Re}(F(s))}$	$P_{\text{Im}(F(s))}$
0.9260	0.9277	0.9265
0.9257	0.9265	0.9261
0.9245	0.9249	0.9248
0.8987	0.8967	0.8951

**Table 3.** Porosity  $P$  recovered from the real part of function  $F(s)$ . Noise added to the real part of complex conductivity is indicated in % of noise (mean  $\pm$  standard deviation).

$P_{\text{true}}$	$P_{\text{Recovered}}$	Noise $_{\sigma_2}$	Noise $_{\sigma_1}$	Noise $_{\sigma_{\text{eff}}^*}$
0.9260	0.9544	3.74 $\pm$ 2.98	3.89 $\pm$ 2.67	1.85 $\pm$ 1.48
0.9260	0.9459	14.55 $\pm$ 13.77	16.51 $\pm$ 14.07	3.08 $\pm$ 2.43
0.9260	0.9323	33.45 $\pm$ 28.20	28.60 $\pm$ 12.81	2.89 $\pm$ 2.55
0.9260	0.9119	42.88 $\pm$ 29.38	29.33 $\pm$ 26.29	2.52 $\pm$ 1.87
0.9257	0.9150	8.14 $\pm$ 4.75	6.11 $\pm$ 4.86	2.25 $\pm$ 1.79
0.9257	0.9271	17.13 $\pm$ 15.03	17.11 $\pm$ 11.17	2.01 $\pm$ 1.93
0.9257	0.9260	26.76 $\pm$ 22.56	26.69 $\pm$ 11.95	3.38 $\pm$ 2.97
0.9257	0.9578	30.61 $\pm$ 14.816	23.65 $\pm$ 21.38	2.75 $\pm$ 2.10
0.9245	0.9195	2.43 $\pm$ 1.99	2.93 $\pm$ 1.57	2.41 $\pm$ 1.68
0.9245	0.9008	12.21 $\pm$ 7.13	9.17 $\pm$ 7.30	2.25 $\pm$ 1.78
0.9245	0.9146	28.30 $\pm$ 20.76	38.08 $\pm$ 23.92	2.05 $\pm$ 1.99
0.9245	0.9586	44.77 $\pm$ 24.89	33.94 $\pm$ 23.44	1.69 $\pm$ 2.12
0.8987	0.8956	2.43 $\pm$ 1.99	2.93 $\pm$ 1.57	2.41 $\pm$ 1.68
0.8987	0.8987	8.14 $\pm$ 4.75	6.11 $\pm$ 4.86	2.24 $\pm$ 1.78
0.8987	0.9312	21.52 $\pm$ 19.86	30.02 $\pm$ 13.37	2.49 $\pm$ 1.86
0.8987	0.9215	22.34 $\pm$ 19.61	25.67 $\pm$ 16.75	2.01 $\pm$ 1.93

model the uncertainty in the real and imaginary parts of the properties of the constituents and possible experimental errors in the measurements of effective properties. The reconstruction algorithm developed in section 3 was implemented in Matlab to recover the spectral function  $\eta$ . Then, porosity  $P$  of bone was calculated using (13). We want to emphasize that the term ‘noise’ means error added to the values of the properties used in the inversion algorithm presented in section 3 to account for possible uncertainty in the estimation of the conductivity of the bone components and measurement error.

#### 4.3. Results and discussion

Table 2 shows the recovered porosity for four different specimens of trabecular bone, similar to that whose micro-CT image is shown in figure 1. The specimens have slightly different porosity shown in the left column of the table. True porosity of the sample was determined digitally from the micro-CT scan. The next two columns contain values of porosity reconstructed from the effective complex conductivity using the algorithm presented. The values of complex conductivity in this case are transformed to the function  $F(s)$ , and the real and imaginary parts of function  $F(s)$  are used as an input for the algorithm. This series of simulations uses data without any additional noise added; only computational noise is present. This corresponds to the case when measured effective conductivity has no (or very small) experimental error and complex conductivity of trabecular tissue and bone marrow are known exactly. The table separately shows the porosity reconstructed from the real and imaginary parts of function

**Table 4.** Porosity  $P$  recovered from the imaginary part of function  $F(s)$ . Noise added to the imaginary part of complex conductivity is given in % of noise (mean  $\pm$  standard deviation).

$P_{\text{true}}$	$P_{\text{Recovered}}$	Noise $_{\sigma_2}$	Noise $_{\sigma_1}$	Noise $_{\sigma_{\text{eff}}^*}$
0.9260	0.9151	4.71 $\pm$ 3.29	5.17 $\pm$ 3.4	1.92 $\pm$ 2.04
0.9260	0.9026	13.89 $\pm$ 13.30	14.17 $\pm$ 9.21	1.88 $\pm$ 1.52
0.9260	0.9290	17.78 $\pm$ 14.27	27.95 $\pm$ 14.96	2.75 $\pm$ 1.68
0.9260	0.8828	29.25 $\pm$ 26.55	33.68 $\pm$ 27.39	2.45 $\pm$ 1.78
0.9257	0.9367	6.46 $\pm$ 4.37	9.23 $\pm$ 6.58	2.83 $\pm$ 1.97
0.9257	0.9189	15.53 $\pm$ 10.21	9.61 $\pm$ 10.21	2.51 $\pm$ 1.52
0.9257	0.9317	13.63 $\pm$ 10.94	22.36 $\pm$ 11.97	2.75 $\pm$ 1.68
0.9257	0.9190	15.53 $\pm$ 10.21	9.61 $\pm$ 10.21	3.34 $\pm$ 2.02
0.9245	0.9328	10.35 $\pm$ 6.80	6.40 $\pm$ 6.80	2.51 $\pm$ 1.52
0.9245	0.9015	13.89 $\pm$ 13.30	17.71 $\pm$ 11.52	1.88 $\pm$ 1.52
0.9245	0.9146	20.75 $\pm$ 16.65	33.54 $\pm$ 17.96	2.75 $\pm$ 1.68
0.9245	0.9099	31.14 $\pm$ 21.28	30.91 $\pm$ 21.53	1.47 $\pm$ 0.90
0.8987	0.8896	3.48 $\pm$ 1.95	3.67 $\pm$ 3.11	2.10 $\pm$ 1.30
0.8987	0.9298	6.46 $\pm$ 4.37	9.23 $\pm$ 6.57	2.83 $\pm$ 1.97
0.8987	0.8998	15.53 $\pm$ 10.21	9.61 $\pm$ 10.21	2.51 $\pm$ 1.52
0.8987	0.8849	13.89 $\pm$ 13.30	17.71 $\pm$ 11.52	1.89 $\pm$ 1.52

**Table 5.** Porosity  $P_{\text{Re}(F(s))}$  recovered from the real part of function  $F(s)$  for data sets consisting of five data points. Noise added to the complex conductivity values is indicated in % of noise (mean  $\pm$  standard deviation).

$P_{\text{True}}$	$P_{\text{Re}(F(s))}$	Noise $_{\text{Re}(\sigma_1)}$	Noise $_{\text{Im}(\sigma_1)}$	Noise $_{\text{Re}(\sigma_2)}$	Noise $_{\text{Im}(\sigma_2)}$	Noise $_{\text{Re}(\sigma^*)}$
0.9257	0.9339	0	0	0	0	
0.9257	0.9188	4.36 $\pm$ 2.23	3.29 $\pm$ 2.97	5.28 $\pm$ 4.68	3.64 $\pm$ 3.15	2.78 $\pm$ 2.34
0.9257	0.9591	7.68 $\pm$ 5.05	10.39 $\pm$ 7.95	7.80 $\pm$ 4.28	5.39 $\pm$ 4.38	2.76 $\pm$ 2.44
0.9257	0.9386	12.64 $\pm$ 10.91	15.95 $\pm$ 11.59	12.70 $\pm$ 9.82	13.63 $\pm$ 8.57	2.14 $\pm$ 1.92
0.9257	0.9303	20.32 $\pm$ 14.41	8.68 $\pm$ 7.85	7.97 $\pm$ 6.62	16.30 $\pm$ 12.45	4.13 $\pm$ 3.44
0.9257	0.9221	12.97 $\pm$ 8.78	16.82 $\pm$ 10.60	15.81 $\pm$ 12.26	14.16 $\pm$ 9.92	2.83 $\pm$ 1.90

$F(s)$  in the columns with headings  $P_{\text{Re}(F(s))}$  and  $P_{\text{Im}(F(s))}$ . Results of numerical reconstruction presented in the table show that in this case, the porosity is recovered very accurately with an error less than 0.1%.

Tables 3 and 4 show porosity recovered from the real and imaginary parts of function  $F(s)$  constructed from the data containing noise. Noise levels are reported as a mean and standard deviation over a range of frequencies for each specimen. Horizontal lines separate results for different samples. Results of computational experiments show stability of the reconstruction. Even with high level noise in the simulated data, the recovered values of porosity are close to the true values.

The previous results were obtained using 11 data points in a  $10 - 10^{11}$  Hz frequency range. The next series of computations was performed to verify that a smaller data set would be sufficient to use in reconstruction. We used 4, 5 or 6 data points in the range from 10 Hz to 1 MHz with satisfactory accuracy. Table 5 shows bone porosity recovered from effective data given at five frequencies. The numerical simulations confirm that even such a small data set provides sufficient information for stable reconstruction of porosity values.

Solutions reconstructed using the regularization technique, depend on the regularization parameter  $\alpha$  which was chosen using the L-curve method. Figure 4 shows a typical curvature curve (left figure) and a L-shaped curve (right figure) corresponding to the reconstruction

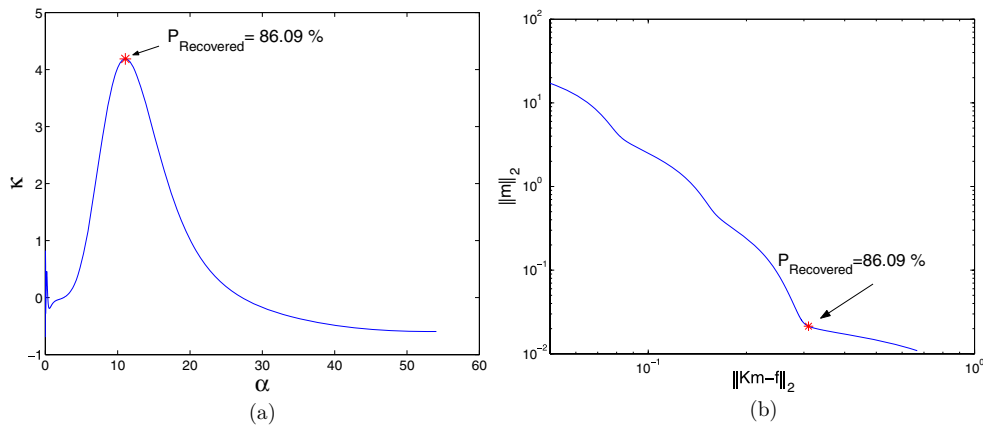


**Figure 4.** Example of curvature and L-shaped curves calculated in inversion of the real part of function  $F(s)$ .  $P_{\text{True}} = 0.8987$  and  $P_{\text{Recovered}} = 0.8609$ ; noise levels of  $20.35 \pm 11.88$ ,  $12.22 \pm 9.72$  and  $2.24 \pm 1.78$  for  $\sigma_2$ ,  $\sigma_1$  and  $\sigma_{\text{eff}}^*$ , respectively. (a) Curvature  $\kappa$  versus the regularization parameter  $\alpha$ ; star \* marks the point of maximum of the curvature and corresponds to a recovered porosity of 0.86. (b) Euclidean norm of solution  $\|m\|_2$  versus the Euclidean norm of the residual  $\|Km - f\|_2$  in the logarithmic scale; star \* denotes the point corresponding to the maximum curvature.

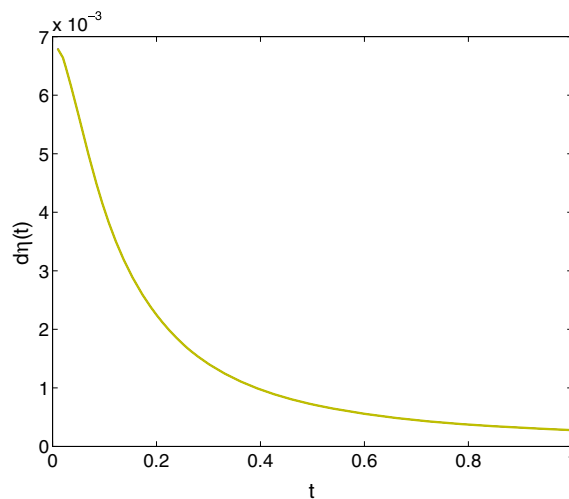


**Figure 5.** Reconstructed function  $d\eta(t)$  corresponding to point of maximum curvature for example given in figure 4.

algorithm for the real part of  $F(s)$ . The porosity recovered for the regularization parameter corresponding to the point of maximal curvature is close to the true porosity even though the properties of the constituents contained a mean error of 20% and 12%, respectively. For this particular case, figure 5 shows the reconstructed function  $d\eta$  calculated for the regularization parameter corresponding to maximal curvature. The reconstructed function  $d\eta$  is very smooth without discontinuities or big jumps as is expected for solutions constructed using this type of regularization.

We note that healthy cancellous bone has porosity levels between 30% and 60% depending on the type of bone and around or above 90% for osteoporotic bone (Qin *et al* 2007). In compact bone, studies have shown an increase of porosity of 41% in fracture cases compared with healthy ones (control group) (Bell *et al* 1999). The results of numerical simulations show that even with high percent of error in the estimation of properties of the constituents, the algorithm was able to recover an accurate approximation of the true porosity of bone with an error of 2–3%. This justifies our conclusion that the developed method has sufficient accuracy to register porosity levels relevant to osteoporosis.

## 5. Conclusions

In this paper, we have shown the potential of using the spectral representation of effective properties in recovering bone porosity. This representation is analytical; it does not depend on correlation analysis. Conventional approaches either rely on correlation analysis or require a forward model of the micro-architecture of bone in terms of relevant parameters such as constituents, relative volume fractions and geometrical parameters. It is extremely difficult to create accurate forward models of the morphology of a heterogeneous medium such as bone. The spectral representation however is unique and does not require any model of the bone morphology.

The spectral function can be used to find the effective behavior of heterogeneous material, it also contains important information about the microgeometry of bone such as volume fraction of constituents. In this work, we have shown the future potential of the spectral function to help to understand and address issues of clinical relevance such as porosity levels in bone. We developed a method which allows us to derive bone porosity from experimental measurements of complex conductivity over a range of frequencies. On the other hand, exploitation of the rich information enclosed in the spectral representation is not simple. It requires to use regularization techniques to deal with numerical instabilities due to the ill-conditioned character of the problem. A numerical scheme involving the regularization method depends on a regularization parameter  $\alpha$ . The success of the method is determined by the ability to choose an appropriate value for parameter  $\alpha$ . The L-curve criterion is a common method used to adjust the regularization parameter when Tikhonov filters are employed. We have shown that this criterion works well for the current problem even with a large level of noise in the numerically simulated data. The presented method has been validated using 2D micro-CT scans of trabecular bone. However, the method is completely general and valid for a three-dimensional problem. This study shows the potential of electrical spectroscopy to address porosity levels in bone for monitoring anti-osteoporotic treatment.

## Acknowledgments

We would like to thank Professor Yener N Yeni and his group, especially Dr Janardhan Yerramshetty, for providing micro-CT images of cancellous bone that we used in our numerical simulations. This work was supported by NSF grant DMS-0508901.

## Appendix A

In this section, we will derive the Stieltjes representation of the effective complex conductivity of a heterogeneous medium using homogenization theory (two-scale asymptotic expansion). To model fine scale bone properties we introduce a small parameter  $\epsilon$  characterizing the

structure on the microscale. We start with the equation in terms of the complex conductivity tensor in the Fourier domain given in (7) and rewritten here as

$$\operatorname{div} \sigma^\epsilon \mathbf{E}^\epsilon = 0. \tag{A.1}$$

To simplify the notation, we have dropped the star symbol for the complex conductivity and used notation  $\operatorname{div}$  for the divergence operator ( $\nabla \cdot$ ). It is assumed that the distribution of the heterogeneities is periodic on the microscale. We introduce another spatial variable  $\mathbf{y}$  to characterize the distribution of the heterogeneities on the fine scale,  $\mathbf{y} = \mathbf{x}/\epsilon$ , so that  $\sigma^\epsilon(\mathbf{x}/\epsilon) = \sigma(\mathbf{y})$ . Here  $\epsilon$  is a small positive parameter such that the complex conductivity  $\sigma^\epsilon$  is now a known periodic function of periods  $Y$  and  $\epsilon Y$  in the microscopic ( $\mathbf{y}$ -scale) and macroscopic ( $\mathbf{x}$ -scale) scales, respectively. We look for an asymptotic solution for (A.1) of the form

$$\phi^\epsilon(\mathbf{x}) = \phi(\mathbf{x}, \mathbf{y}) = \phi^0(\mathbf{x}) + \epsilon \phi^1(\mathbf{x}, \mathbf{y}) + \epsilon^2 \phi^2(\mathbf{x}, \mathbf{y}) + \dots \tag{A.2}$$

The electric field  $\mathbf{E}^\epsilon$  can be written in terms of a potential function  $\phi^\epsilon$  as  $\mathbf{E}^\epsilon = \nabla \phi^\epsilon$ . The divergence  $\operatorname{div}$  and gradient  $\nabla$  operators are expressed as

$$\operatorname{div} = \frac{1}{\epsilon} \operatorname{div}_y + \operatorname{div}_x \quad \nabla = \frac{1}{\epsilon} \nabla_y + \nabla_x. \tag{A.3}$$

Using these expressions, we obtain asymptotic expansions for the electric field  $\mathbf{E}^\epsilon$  and for the current density field  $\mathbf{J}^\epsilon$ . The expansion for the electric field is of the form

$$E_j^\epsilon = E_j^0 + \epsilon E_j^1 + \epsilon^2 E_j^2 + \dots \tag{A.4}$$

where  $E_j$  represents the  $j$ th component of vector  $\mathbf{E}$ , and

$$E_j^n = \frac{\partial}{\partial x_j} \phi^n + \frac{\partial}{\partial y_j} \phi^{n+1} \quad \text{for } n = 0, 1, 2, \dots \tag{A.5}$$

For the current density field,  $\mathbf{J}^n = \sigma \mathbf{E}^n$  for  $n = 0, 1, 2, \dots$ , and the expansion has the form

$$J_i^\epsilon = J_i^0 + \epsilon J_i^1 + \epsilon^2 J_i^2 + \dots \tag{A.6}$$

Substituting the asymptotic expansions given by (A.6) into (A.1) and taking the limit as  $\epsilon \rightarrow 0$ , we obtain two problems at different scales. The problem at the macroscale ( $\epsilon^0$ ) is

$$\operatorname{div}_x J^0 + \operatorname{div}_y J^1 = 0. \tag{A.7}$$

At the microscale ( $\epsilon^1$ ), we have the local problem

$$\operatorname{div}_y J^0 = \operatorname{div}_y (\sigma (\nabla_x \phi^0 + \nabla_y \phi^1)) = 0. \tag{A.8}$$

The solution of the local problem is given by

$$\phi^1(\mathbf{x}, \mathbf{y}) = - \sum_{j=1}^3 \Phi_j(\mathbf{y}) \frac{\partial}{\partial x_j} \phi^0 + A(\mathbf{x}), \tag{A.9}$$

where  $A(\mathbf{x})$  is a constant function in the  $\mathbf{y}$  scale. Function  $\Phi(\mathbf{y}) = (\Phi_1, \Phi_2, \Phi_3)$  is a  $Y$ -periodic function, and each component  $\Phi_k$  satisfies the following variational problem:

$$\int_Y \sigma \nabla_y \Phi_k \cdot \nabla_y \Psi \, dy = \int_Y \sigma \nabla_y \Psi \, dy \tag{A.10}$$

for every periodic function  $\Psi(\mathbf{y})$  that belongs to a local Sobolev space  $V_Y$  of periodic functions with zero average over the periodic cell. More explicit mathematical details can be found in chapter 7 in Cioranescu and Donato (1999). Using periodicity conditions and applying the divergence theorem, we obtain from (A.10)

$$\operatorname{div}_y (\sigma \nabla_y (\Phi_k + y_k)) = 0 \quad \text{for } k = 1, 2, 3. \tag{A.11}$$

Here  $\sigma$  is the second-order tensor of the complex conductivity properties of the heterogeneous material. In numerical simulations, we assume that the heterogeneous material is transversely isotropic in the  $y$ -scale with  $y_3$  being the axis of symmetry, so that  $\sigma_{11} = \sigma_{22}$ . Using the fact that  $\sigma(\mathbf{y}) = h\chi(\mathbf{y}) + (1 - \chi(\mathbf{y}))$  where  $\chi$  is the characteristic function of the composite and  $h = \sigma_1/\sigma_2$  with  $\sigma_i$  being the complex conductivity of material  $i$ , equation (A.11) is reduced to

$$\nabla_y \cdot \chi (\nabla_y \Phi_k + e_k) = s \Delta_y \Phi_k. \quad (\text{A.12})$$

Here  $s = 1/(1 - h)$  and  $e_k$  is the unit ort along the axis  $y_k$ . Then, using algebra manipulation, we obtain from (A.12)

$$E = s(sI + \Gamma\chi)^{-1}e_k, \quad (\text{A.13})$$

where  $\Gamma = \nabla_y(-\Delta)^{-1}\nabla_y$  and  $\Delta$  is the Laplace operator with respect to  $\mathbf{y}$ . Using the spectral resolution of operator  $\Gamma\chi$  and assuming that  $\sigma_{\text{eff}}$  is the  $kk$  th component of the measured tensor of effective properties, we obtain the spectral representation for the function  $F(s)$

$$F(s) = 1 - \frac{\sigma_{\text{eff}}(s)}{\sigma_2} = \int_0^1 \frac{d\eta(z)}{s - z}. \quad (\text{A.14})$$

In Golden and Papanicolaou (1983) and Cherkaev (2001), more detailed steps of the derivation are provided.

## Appendix B

In this section, we will outline a semi-analytical method to calculate the effective properties of cancellous bone for an idealized microstructure formed by the hexagonal lattice of circular cylinders of radius  $a$  and conductivity  $\sigma_2$  embedded in a matrix of conductivity  $\sigma_1$ . A two-dimensional cross-section of this structure is shown in figure B1. The effective complex conductivity of the cancellous bone's idealized structure is determined with a method proposed by Perrins *et al* (1979).

Symmetries of the geometric structure allow us to reduce the consideration to a 2D problem. We consider a coordinate system  $(x_1, x_2)$  with the origin located at point P (see figure B1). The governing equation (8) is given for inhomogeneous conductivity  $\sigma^*(\mathbf{x})$

$$\nabla \cdot (\sigma^* \nabla \phi) = 0 \quad \text{in } \Omega, \quad \sigma^*(\mathbf{x}) = \chi(\mathbf{x})\sigma_1^* + (1 - \chi(\mathbf{x}))\sigma_2^*. \quad (\text{B.1})$$

Here  $\sigma^*(\mathbf{x})$  is the inhomogeneous conductivity in the domain  $\Omega = \Omega_1 \cup \Omega_2$ ,  $\sigma_i^*$  is the conductivity of phase  $i$  and  $\chi(\mathbf{x})$  is the characteristic function of the domain  $\Omega_1$  so that it takes value 1 if  $\mathbf{x}$  is in phase 1 and 0 otherwise,  $\mathbf{x} = (x_1, x_2)$ . The governing equation can be rewritten as

$$\nabla \cdot (\sigma_1^* \nabla U_1) = 0 \quad \text{in } \Omega_1, \quad \nabla \cdot (\sigma_2^* \nabla U_2) = 0 \quad \text{in } \Omega_2. \quad (\text{B.2})$$

For a constant electric field  $E_0$  applied in the  $x_1$  direction, the solution of the problem for a unit hexagonal cell can be reduced to the solution of the Laplace equation inside and outside of the cylinder. In the polar coordinate system  $(r, \theta)$ , the problem has a solution in terms of Fourier expansions as

$$\phi(r, \theta) = \begin{cases} U_1(r, \theta), & \text{if } r > a, \\ U_2(r, \theta), & \text{if } r < a \end{cases} \quad (\text{B.3})$$

where outside the cylinder, for  $r > a$ , Fourier series for  $U_1$  has the form

$$U_1(r, \theta) = A_0 + (A_1 r + B_1 r^{-1}) \cos \theta + (A_3 r^3 + B_3 r^{-3}) \cos 3\theta + \dots \quad (\text{B.4})$$

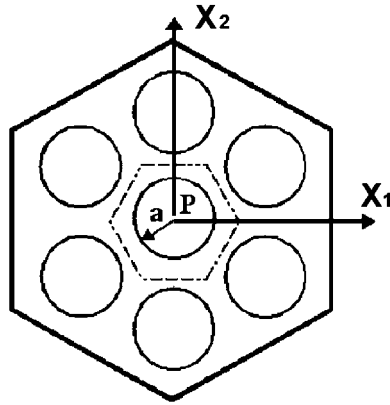


**Figure B1.** 2D section of the hexagonal cylindrical structure used in model simulations to validate the computation of the effective properties of trabecular bone. Cylinders represents trabecular bone tissue embedded in a matrix (bone marrow phase). The overall symmetry in 3D is transversely isotropic.

and inside the cylinder, for  $r < a$ , Fourier series for  $U_2$  is

$$U_2(r, \theta) = C_0 + C_1 r \cos \theta + C_3 r^3 \cos 3\theta + \dots \quad (\text{B.5})$$

Boundary conditions at the interface ( $r = a$ ) are given by the continuity of the electrical and the displacement fields

$$U_1(a, \theta) = U_2(a, \theta), \quad \gamma \frac{\partial U_2(a, \theta)}{\partial n} = \frac{\partial U_1(a, \theta)}{\partial n}, \quad (\text{B.6})$$

where  $\gamma = \sigma_2^* / \sigma_1^*$ .

Boundary conditions can be used to work out relations between the coefficients of the Fourier expansions (B.4) and (B.5). The contribution to the potential  $\phi(x_1, x_2)$  at the point  $(x_1, x_2)$  due to the multiple inclusions (excluding the cylinder at P) is given by the cosine series (B.4) corresponding to the series

$$A_0 + (A_1 - E_0)(x_1 + ix_2) + A_3(x_1 + ix_2)^3 + \dots \quad (\text{B.7})$$

An equivalent expression might be obtained if we sum up all contributions of the other cylinders with centers at  $Q_n$ ,  $Q_n \neq P$

$$\sum_{Q_n} (B_1(x'_1 + ix'_2)^{-1} + B_3(x'_1 + ix'_2)^{-3} + \dots), \quad (\text{B.8})$$

where  $x'_1$  and  $x'_2$  are the coordinates of the same point  $(x_1, x_2)$  referred to the center  $Q_n$  of the corresponding cylinder. Equivalence of expressions (B.7) and (B.8) results in a system of equations which together with equations (B.6) gives us a relation between  $E_0$  and  $B_1$  (Lord 1892). For a hexagonal array of cylinders, it is convenient to use the symmetry of the structure and consider two additional fields in the directions  $(-1/2, -1/2\sqrt{3})$  and  $(-1/2, 1/2\sqrt{3})$ , so that the total field is zero (Perrins *et al* 1979). If  $U_1(r, \theta)$  is the potential due to  $E_0$ , then  $U_1(r, \theta) + U_1(r, \theta + 2/3\pi) + U_1(r, \theta + 4/3\pi) = 0$ . Using expression (B.4), we find

$$\sum_l (A_l r^l + B_l r^{-l}) \cos l\theta (1 + 2 \cos 2/3\pi l) = 0. \quad (\text{B.9})$$

This relation together with equivalence between (B.7) and (B.8) results in the following system of linear equations for the coefficients  $B_{2n-1}$

$$E_0 \delta_{n1} - (2n-1)! \frac{(1+\gamma)B_{2n-1}}{(1-\gamma)a^{4n-2}} = \sum_{m=1,2,\dots} \frac{(2n+2m-3)!}{(2m-2)!} S_{2n+2m-2} B_{2m-1}, \quad (\text{B.10})$$

where  $\delta_{n1}$  is the Kronecker delta symbol,  $a$  is the radius of the cylinders. In (B.10),  $S_l$  is given by

$$S_l = \sum_{j=1}^{\infty} (x_1^{(j)} + ix_2^{(j)})^{-1}, \quad (\text{B.11})$$

where  $(x_1^{(j)}, x_2^{(j)})$  are the coordinates  $(x_1, x_2)$  of the center of the  $j$ th cylinder for all cylinders except that centered at point P. Applying the second Green's identity to the unit cell (figure B1) we obtain the effective conductivity property given by

$$\sigma_{\text{eff}}^* = 1 - 4\pi \frac{B_1}{\sqrt{3}} E_0 \quad (\text{B.12})$$

and  $B_1$  is determined by solving (B.10).

Note that the effects of porosity in the effective conductivity are introduced into the equation through the Fourier coefficient  $B_1$ ; indeed, the system of linear equations (B.10) depends on the radius  $a$  of the cylinders. The solution of this system also depends on the ratio of the properties  $\gamma$ , and hence the effective complex conductivity also depends on frequency if the constituents of cancellous bone have frequency-dependent conductivity values.

## References

- Bell K L, Loveridge N, Power J, Garrahan N, Meggitt B F and Reeve J 1999 Regional differences in cortical porosity in the fractured femoral neck *Bone* **24** 57–64
- Bergman D J 1978 The dielectric constant of a composite material—a problem in classical physics *Phys. Rep. C* **43** 377–407
- Bergman D J 1980 Exactly solvable microscopic geometries and rigorous bounds for complex dielectric constant of a two-component composite material *Phys. Rev. Lett.* **44** 1285–7
- Bergman D J 1985 Bulk physical properties of composite media *Les Méthodes de L'homogénéisation: Théorie et Applications en Physique (Collection de la Direction des Études et Recherches D'Électricité de France)* (Paris: Editions Eyrolles) pp 1–128
- Bergman D J 1993 Hierarchies of Stieltjes functions and their applications to the calculation of bounds for the dielectric constant of a two-component composite medium *SIAM J. Appl. Math.* **53** 915–30
- Bonifasi-Lista C and Cherkaev E 2006 Identification of bone microstructure from effective complex modulus *Vibration Problems ICOVP 2005 (Springer Proceedings in Physics vol 111)* ed E Inan and A Kiris pp 91–6
- Bonifasi-Lista C and Cherkaev E 2008 Analytical relations between effective material properties and microporosity: application to bone mechanics *Int. J. Eng. Sci.* **46** 1239–52
- Cioranescu D and Donato P 1999 *An Introduction to Homogenization (Oxford Lectures Series in Mathematics and its Applications)* (London: Oxford University Press)
- Cherkaev E 2001 Inverse homogenization for evaluation of effective properties of a mixture *Inverse Problems* **17** 1203–18
- Cherkaev E 2003 Spectral coupling of effective properties of a random mixture *IUTAM Symp. on Asymptotics, Singularities and Homogenisation in Problems of Mechanics* ed A B Movchan (Dordrecht: Kluwer) pp 331–40
- Cherkaev E and Golden K 1998 Inverse bounds for microstructural parameters of a composite media derived from complex permittivity measurements *Waves Random Media* **8** 437–50
- Cherkaeva E and Tripp A C 1996 Bounds on porosity for dielectric logging *Proc. of the 9th Conf. of the European Consortium for Mathematics in Industry* (Technical University of Denmark, Copenhagen)
- Cherkaev E and Ou M J 2008 De-homogenization: reconstruction of moments of the spectral measure of composite *Inverse Problems* **24** 065008
- Cherkaev E and Zhang D 2003 Coupling of the effective properties of a random mixture through the reconstructed spectral representation *Phys. B: Phys. Condens. Matter* **338** 16–23

- Day A R and Thorpe M F 1999 The spectral function of a composite: the inverse problem *J. Phys. Condens. Matter* **11** 2551–68
- Day A R, Thorpe M F, Grant A R and Sievers A J 2000 The spectral function of a composite from reflectance data *Physica B* **279** 17–20
- Gabriel C, Gabriel S and Corthout E 1996a The dielectric properties of biological tissues: I. Literature survey *Phys. Med. Biol.* **41** 2231–49
- Gabriel S, Lau R W and Gabriel C 1996b The dielectric properties of biological tissues: II. Measurements in the frequency range of 10 Hz to 20 GHz *Phys. Med. Biol.* **41** 2251–69
- Gabriel S, Lau R W and Gabriel C 1996c The dielectric properties of biological tissues: III. Parametric models for the dielectric spectrum of tissues *Phys. Med. Biol.* **41** 2271–93 Software for calculation of dielectric properties of tissues available at <http://niremf.ifac.cnr.it/tissprop/>
- Gajdardziska-Josifovska M, McPhedran R C, Cockayne D J H, McKenzie D R and Collins R E 1989a Silver-magnesium fluoride cermet films: I. Preparation and microstructural and electrical properties *Appl. Opt.* **28** 2736–43
- Gajdardziska-Josifovska M, McPhedran R C, Cockayne D J H, McKenzie D R and Collins R E 1989b Silver-magnesium fluoride cermet films: II. Optical and electrical properties *Appl. Opt.* **28** 2736–53
- Golden K M, Ackley S F and Lytle V I 1998 The percolation phase transition in sea ice *Science* **282** 2238–41
- Golden K and Papanicolaou G 1983 Bounds for the effective parameters of heterogeneous media by analytic continuation *Commun. Math. Phys.* **90** 473–91
- Golden K and Papanicolaou G 1985 Bounds for effective parameters of multicomponent media by analytic continuation *J. Stat. Phys.* **40** 655–67
- Habal M B and Reddi A H 1992 *Bone Grafts and Bone Substitutes: Investigation and Clinical Application* (Philadelphia, PA: Saunders)
- Hashin Z 1972 Theory of fiber reinforced materials *NASA Contractor Report* NASA CR-1974
- Hernandez C J 2006 A biomechanical perspective on bone quality *Bone* **39** 1173–81
- Katz S, Zlochiver S and Abboud S 2006 Induced current bio-impedance technique for monitoring bone mineral density—a simulation model *Ann. Biomed. Eng.* **34** 1332–42
- Lax P D 2002 *Functional Analysis* (New York: Wiley)
- Lord Rayleigh 1892 On the influence of obstacles arranged in rectangular order upon the properties of a medium *Phil. Mag.* **34** 481–502
- McPhedran R C, McKenzie D R and Milton G W 1982 Extraction of structural information from measured transport properties of composites *Appl. Phys. A* **29** 19–27
- McPhedran R C and Milton G W 1990 Inverse transport problems for composite media *Mater. Res. Soc. Symp. Proc.* **195** 257–74
- Milton G W 1979 Theoretical studies of the transport properties of inhomogeneous media *Research Project Report* (Sidney: University of Sidney)
- Milton G W 1980 Bounds on the complex dielectric constant of a composite material *Appl. Phys. Lett.* **37** 300–2
- Milton G W 1981 Bounds on the complex permittivity of a two-component composite material *J. Appl. Phys.* **52** 5286–93
- Milton G W and Golden K 1990 Representations for the conductivity functions of multicomponent composites *Commun. Pure Appl. Math.* **43** 5 647–71
- Perrins W T, McKenzie D R and McPhedran R C 1979 Transport properties of regular arrays of cylinders *Proc. R. Soc. Lond. A* **369** 207–25
- Prins S H, Jørgensen H L, Jørgensen L V and Hassanger C 1998 The role of quantitative ultrasound in the assessment of bone: a review *Clin. Physiol. Funct. Imaging* **18** 3–17
- Qin L, Genant H K, Griffith J and Leung K-S 2007 *Advanced Bioimaging Technologies in Assessment of the Quality of Bone and Scaffold Materials: Techniques and Applications* (Berlin: Springer)
- Sierpowska J, Hakulinen M A, Töyräs J, Day J S, Weinans H, Jurvelin J S and Lappalainen R 2005 Prediction of mechanical properties of human trabecular bone by electrical measurements *Physiol. Meas.* **26** S119–31
- Sierpowska J, Lammi M J, Hakulinen M A, Jurvelin J S, Lappalainen R and Töyräs J 2007 Effect of human trabecular bone composition on its electrical properties *Med. Eng. Phys.* **29** 845–52
- Sierpowska J, Töyräs J, Hakulinen M A, Saarakkala S, Jurvelin J S and Lappalainen R 2003 Electrical and dielectrical properties of bovine trabecular bone—relationship with mechanical properties and mineral density *Phys. Med. Biol.* **48** 775–86
- Speller R D, Royle G J and Horrocks J A 1989 Instrumentation and techniques in bone density measurement *J. Phys. E: Sci. Instrum.* **22** 202–14
- Tokarzowski S, Telega J J and Galka A 2001 Torsional rigidities of cancellous bone filled with marrow: the application of multipoint Pade approximants *Eng. Trans.* **49** 135–53

- Tripp A C, Cherkaeva E and Hulen J 1998 Bounds on the complex conductivity of geophysical mixtures *Geophys. Prospect.* **46** 589–601
- Tuncer E 2005 Extracting the spectral density function of a binary composite without a priori assumptions *Phys. Rev. B* **71** 012101
- Vogel C R 2002 *Computational Methods for Inverse Problems* (Philadelphia, PA: SIAM)
- Williams P A and Saha S 1996 The electrical and dielectric properties of human bone tissue and their relationship with density and bone mineral content *Ann. Biomed. Eng.* **24** 223–33
- Zhang D and Cherkaev E 2008 Pade approximations for identification of air bubble volume from temperature or frequency dependent permittivity of a two-component mixture *Inverse Problems Sci. Eng.* **16** 425–45